Jule Kersebaum[1,2]
Steffen Flaischlen[1]
Julia Hofinger[3]
Gregor D. Wehinger[1,4,*]

Simulating Stirred Tank Reactor Characteristics with a Lattice Boltzmann CFD Code

Supporting Information available online

Although mixing in stirred tanks is common in the chemical and process industry, it is complex and not fully understood. In recent years, computational fluid dynamics (CFD) simulations with large eddy simulation turbulence models have become an important modeling tool. In this study, its current state for applicability to stirred tanks was evaluated. First, the power characteristics of different impellers were simulated and compared with experimental data. Second, Rushton and pitched blade turbines were validated in terms of the local velocity components, dissipation rates, and the trailing vortex. Finally, mixing times for different viscosity ratios were obtained from the CFD results and compared with a literature study. Hydrodynamics can be well predicted. However, mixing times for viscosity ratios larger than 1:100 are error-prone.

1   Introduction

User-friendly, fast, and reliable prediction of fluid dynamic behavior and mixing times for stirred tanks is of high industrial relevance, in particular for scale-up. Considering the high prevalence of agitated tanks as chemical reactors and fermenters, optimization of reaction conditions and reliable scale-up are crucial [1]. Given the wide availability of relatively inexpensive computational resources, it was natural to use experimental validation data from small-scale experiments and perform computational fluid dynamics (CFD) simulations for scale-up, or even skip the validation step if best practices and validations for relevant phenomena can be found in the literature. Until today, however, CFD has mainly been a tool for experienced users, especially in the case of more complex physical contexts such as multiphase flows [2]. Fast and efficient application of classical CFD codes requires practice in meshing and a good understanding of the available models, including their limitations. There has been progress in experimental characterization of flow fields and mixing [3–5] and mixing time measurements in stirred tanks, with which corresponding correlations have been developed [6, 7], even considering advanced methods for CFD [8]. In addition, difficult phenomena such as turbulence are becoming better understood [9–11].

A typically used CFD approach is the finite volume method (FVM) [12], which discretizes the computational domain into a finite number of cells, in which the Navier-Stokes equations are solved. With increasing complexity (but realism) of the problem, such as blending of fluids with significantly different fluid properties, the fast approach of using FVM in combina-

tion with Reynolds-averaged Navier-Stokes (RANS) turbulence models to compute a steady-state flow field and run scalar transport on the frozen flow field and similar logics are becoming inaccurate [13]. Viscosity and density differences in additives and bulk flow or transient flow field due to rotor-stator interaction should be included in the model but increase computation time significantly. Large eddy simulations (LES) could be used instead to simulate the turbulent flow field via low-pass filtering of the Navier-Stokes equations [14]. However, in the framework of FVM, LES is computationally expensive. Therefore, this current work aims to evaluate a different modeling approach for such problems in stirred tanks.

As an alternative approach, the lattice Boltzmann method (LBM) has been found in academia for years [15–17] with

[1]Jule Kersebaum, Steffen Flaischlen, Prof. Dr.-Ing. Gregor D. Wehinger
https://orcid.org/0000-0002-1774-3391
Institute of Chemical and Electrochemical Process Engineering, Clausthal University of Technology, Leibnizstr. 16, 38678 Clausthal-Zellerfeld, Germany.

[2]Jule Kersebaum
Department of Chemical Engineering, University of Chemistry and Technology Prague, Technická 3, 160 00 Praha 6-Dejvice, Czech Republic.

[3]Dr. Julia Hofinger
BASF SE, Carl-Bosch-Straße 38, 67056 Ludwigshafen am Rhein, Germany.

[4]Prof. Dr.-Ing. Gregor D. Wehinger (gregor.wehinger@kit.edu)
Institute of Chemical Process Engineering, Karlsruhe Institute of Technology, Fritz-Haber-Weg 2, 76131 Karlsruhe, Germany.

applications ranging from single-phase advection-diffusion problems to multiphase flows and fluid-structure interactions [18]. Examples of more prominent general-purpose LBM codes are Ludwig [19], ESPResSo [20], Palabos [21], and OpenLB [22], to name only a few. Some commercial codes, such as SIMULIA PowerFLOW and ProLB, allowed application to aeroacoustics [23, 24] and atmospheric flow problems [25].

Claimed advantages of commercial LBM codes compared to FVM codes are simple to no meshing, computational robustness, minimal numerical diffusion, and good parallelization performance. Application to stirred tanks was demonstrated in pioneering work in the early 2000s [26, 27], but the use of in-house codes or specialized commercial codes did not lead to a wider use of LBM for stirred tanks, let alone in industrial application. The development of a versatile commercial LBM code (M-Star CFD by M-Star Simulations, LLC) and availability of cheap graphics processing units (GPUs), which are particularly well suited for LBM, allow a technological jump towards the aim of cheap computation of advanced physics for stirred tanks even on desktop computers [28].

The aim of this work was to evaluate resolution effects and validate velocity and turbulence fields in several single-phase stirred tank setups against measurement data from the open literature. Hence, the focus is on two agitator types: pitched-blade and Rushton turbines, for which experimental data from various publications were utilized for comparison [11, 29, 30].

On the basis of this foundation, mixing time simulations using LES were evaluated and checked against published experimental data [7]. Mixing behavior in cases with different physical properties of additive and bulk fluid was also simulated using LBM, and also larger viscosity ratios were studied to understand the limitations of the currently available method.

2 Materials and Methods

2.1 Theoretical background

2.1.1 Lattice-Boltzmann Method

By employing the LBM, a numerical approach that involves the discretization of the Boltzmann equation, complex fluid flows can be simulated and studied with high accuracy and computational efficiency. At the mesoscopic level, the dynamics of a fluid can be described by the Boltzmann equation [Eq. (1)]:

$$\frac{\partial f}{\partial t} + \xi_\beta \frac{\partial f}{\partial x_\beta} + \frac{F_\beta}{\rho} \frac{\partial f_\beta}{\partial \xi_\beta} = \Omega(f) \tag{1}$$

In this context, the first two terms signify the distribution function of particles in motion with velocity ξ_β, while the third term elucidates the influence of a force on the velocity [18]. The term $\Omega(f)$ defines the collision operator, which characterizes the local redistribution from the particle distribution function f due to collisions. By discretizing the Boltzmann equation [Eq. (1)] with respect to the discrete velocities

$\vec{a}_i = (a_{ix}, a_{iy}, a_{iz})$, physical space, and time, the lattice Boltzmann equation is derived [Eq. (2)]:

$$f_i(\vec{x} + \vec{a}_i \Delta t, t + \Delta t) = f_i(\vec{x}, t) + \Omega_i(\vec{x}, t) \tag{2}$$

In the three-dimensional scenario of a D3Q15 system, a total of 15 velocities are achieved, covering all possible directions. For this purpose, the computational domain is partitioned into a regular grid in which each grid point in three-dimensional space has exactly 14 neighboring grid points. The generation of a regular grid, which does not adapt to the three-dimensional geometry, is considerably faster than the complex mesh generation required by the FVM. The presence of 15 velocities accounts for the possibility of stationary states, effectively representing the central grid point itself. Within each velocity set, a constant velocity c_s is present, which defines the fundamental connection between pressure p and density ρ [Eq. (3)]:

$$p = \rho \cdot c_s^2 \tag{3}$$

The Chapman-Enskog development establishes the link between the lattice Boltzmann equation and the Navier-Stokes equation. This development provides transport coefficients, such as thermal conductivity and viscosity, as molecular parameters, representing a significant advancement towards the continuum conservation equations. The fluid's kinematic viscosity ν is computed by using the relaxation time τ [Eq. (4)]:

$$\nu = a_s^2 \left(\tau - \frac{\Delta t}{2} \right) \tag{4}$$

The value of τ is critical in determining the rate at which the fluid approaches equilibrium, as it is directly associated with the fluid's viscosity.

2.1.2 Turbulence Modeling

Turbulence is effectively handled in this study by employing LES along with the Smagorinsky-Lilly sub-grid closure model [31]. LES enables the three-dimensional and transient resolution of the Navier-Stokes equations on a large scale, while approximations and models are exclusively utilized for small-scale motions. Consequently, the coarse eddies are transiently simulated through decomposition of the velocity field into a filtered component and a sub-grid component [32].

2.1.3 Free Surface

The modeling of the free surface phenomenon in the stirred tank employs the volume of fluid (VoF) method, a numerical technique specifically designed for tracking and determining the shape of the liquid surface [33]. The VoF method is implemented by using a scalar function, i.e., the fraction function α, which describes the volume of each lattice cell. By tracking the volume fraction of each fluid in every lattice cell, the α value is assigned between 0 and 1, representing the volume fraction of

the two different phases. The relationship between the variable α and the velocity field $\vec{u}$ is given by Eq. (5):

$$\frac{\partial \alpha}{\partial t} + \vec{u} \cdot \nabla \alpha = 0 \qquad (5)$$

The physical properties such as density and viscosity are deduced from the distribution of the phases, with the values being averaged in cells containing both fluids. These derived properties are then utilized to compute a new velocity field using the Navier-Stokes equations.

2.1.3 Modeling of Rotation

For the modeling of the moving object, specifically the stirrer in this case, the immersed boundary method was employed. In this approach, the stirrer is represented as a cloud of Lagrangian points with arbitrary positions that can evolve over time. This is a departure from the lattice positions of the fluid flow field, which remain fixed. The coupling between the fluid lattice and the Lagrangian point cloud is achieved through the application of Newton's second law. To facilitate this coupling, the force exerted on each lattice point surrounding an immersed boundary point is calculated and subsequently applied. This ensures that the fluid velocity at each lattice point matches the velocity of the corresponding immersed boundary point.

2.2 LBM CFD code

The commercial CFD code M-Star CFD (version 3.7.24) developed by M-Star Simulations, LLC was utilized to solve the transient Navier-Stokes equations. The complete discretized LB equation can be separated into two distinct steps: collision and streaming. The collision step, represented by Eq. (6), involves the calculation of mass and momentum conversion, whereby f_1^* describes the distribution after the collision.

$$f_i^*(\vec{x}, t) = f_i(\vec{x}, t) - \frac{\Delta t}{\tau}\left(f_i(\vec{x}, t) - f_i^{eq}(\vec{x}, t)\right) \qquad (6)$$

The collision process involves a straightforward algebraic function used to compute the density ρ and the macroscopic velocity $\vec{u}$. These values are then utilized to determine the equilibrium distribution f_i^{eq} and the distribution after the collision f_i^* [Eq. (7)]. Subsequently, the updated distribution f_i^* is transmitted to neighboring points in the streaming step.

$$f_i(\vec{x} + \vec{a_i}\Delta t, t + \Delta t) = f_i^*(\vec{x}, t) \qquad (7)$$

Once both collision and streaming steps are completed, a time step has passed, and the entire process is repeated. The Courant-Friedrichs-Lewy condition is employed as a crucial stability criterion. It is utilized with the calculated Courant number Co [Eq. (8)]:

$$Co = \frac{|\vec{u}|\Delta t}{\Delta x} \qquad (8)$$

In this context, the physical velocity of the fluid $\vec{u}$ is compared to both the time step Δt and the grid point spacing Δx. When the Co exceeds 1, the physical solution is unable to propagate rapidly enough, potentially resulting in a loss of information or an unstable simulation.

The simulations of this study were conducted with an NVIDIA RTX A4000 GPU with 16 GB of RAM and a total of 6144 CUDA cores based on the NVIDIA Ampere architecture. These CUDA cores were employed for parallel processing of the simulations.

2.3 Numerical Setup

Several different reactor dimensions and impeller types were studied to replicate experiments from the open literature:
- Zlokarnik [29] for the study of power characteristics.
- Wu and Patterson [11] for lattice resolution study and velocity field of a Rushton turbine (RT)-equipped stirred tank.
- Murthy and Joshi [30] for velocity field validation of a pitched-blade turbine (PBT)-equipped stirred tank.
- Mixing time in PBT-equipped stirred tanks [7].

For specific geometric dimensions of the stirred tanks, see the Supporting Information. Tab. S1 lists the relevant data for the power characteristics, and Tab. S2 contains data for velocity field and mixing time simulations. Additionally, a lattice point study was conducted to verify the discretization. The grid sizes used and the results of this study are also documented in the Supporting Information.

2.4 Data Analysis

All simulations were conducted in a transient manner, with a lead time of 5 s selected to achieve a fully developed flow field in the tanks. Subsequently, data for an additional 15 s were collected for the simulation of the velocity field and the power number, and then averaged to obtain the solution for the quasi-stationary flow field. To evaluate the mixing time, a lead time of 5 s was selected, based on the rationale mentioned earlier. Subsequently, the second fluid was introduced and monitored by using three distinct probes (see literature references for details Jones and Ozcan-Taskin [7]). Further information can be found in Sect. S2. To determine the mixing time of the entire tank, the logarithm of the root mean square (RMS) variance was calculated using data from all probes [Eq. (9)].

$$\log\sigma_{RMS}^2 = \log\left\{\frac{1}{3}\left(c_{t,1} - 1\right)^2 + \left(c_{t,2} - 1\right)^2 + \left(c_{t,3} - 1\right)^2\right\} \qquad (9)$$

The normalized probe output $c_{t,1}$ was obtained by dividing the probe output over time by the final concentration [7, 34]. In this study, the attainment of mixing time was defined as reaching 95 % uniformity. The desired mixing quality is achieved when the RMS value reaches $\log[(-0.05)^2] = -2.6$ for the last time [35].

Research Article

3   Results and Discussion

3.1   Power Characteristics

In an initial validation step, the well-documented power characteristics of selected impellers were compared between simulations and experimental data. The power characteristics of different impeller types are shown in Fig. 1. The Power number Po is determined over a wide range of Reynolds numbers Re, covering the laminar, transition, and turbulent flow regimes [Eq. (10)]:

$$Po = \frac{P}{\rho N^3 D^5} \tag{10}$$

with the power on the impeller P, the fluid density ρ, the impeller speed N, and the impeller diameter D. The power was calculated by using the torque M (on the rotating boundaries) and N [Eq. (11)]:

$$P = 2\pi \cdot M \cdot N \tag{11}$$

The Reynolds number Re is defined as Eq. (12):

$$Re = \frac{\rho N D^2}{\mu} \tag{12}$$

where μ is the dynamic viscosity of the fluid.

For the RT, the simulation results of the laminar and turbulent regimes predict the experimental results with high accuracy. For the transition range ($100 < Re < 10000$), a slight over-prediction by the simulation can be observed. For the RT, extensive simulations spanned all relevant Reynolds numbers, with fewer simulations for other impeller types, focusing on select flow regimes. The power numbers for the crossbar and anchor impellers closely match experimental values, with the helical ribbon impeller showing deviations (–25 and 13 %). Overall, it is shown that this LB CFD code can be applied to predict the power number in all industrially relevant flow regimes with only minor deviations from the experimental data.
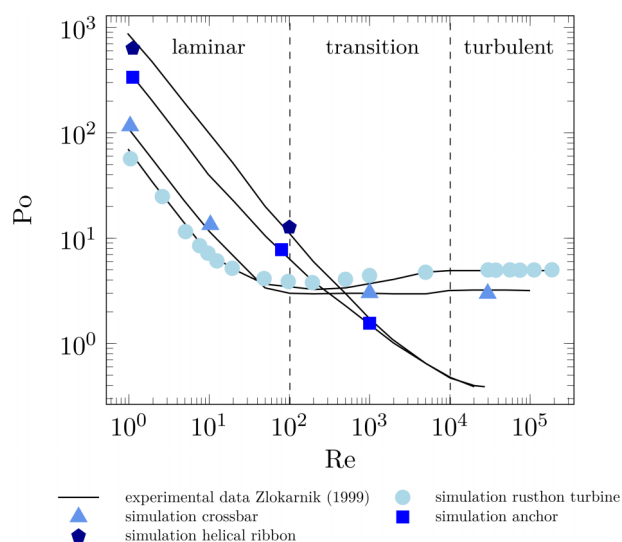

Figure 1. Power characteristics versus Reynolds number for different impeller types and experimental data from the literature [29].

3.2   Flow Fields

3.2.1   Rushton Turbine

A detailed analysis of the obtained CFD results can be performed using local velocity profiles for the RT and PBT. As mentioned in Sect. S1, 300 lattice points over the tank diameter are a sufficient resolution. Fig. 2 shows the velocity profiles for selected radial positions studied in the experimental campaign by Wu and Patterson [11]. The comparison of simulation results with the experimental data for all radial positions is available in the Supporting Information. Radial and tangential profiles closely match experimental data, with potential deviations in axial velocity components due to unmentioned differences in shaft diameter. It is therefore assumed that the shaft in the simulations has a typical diameter of 10 mm.
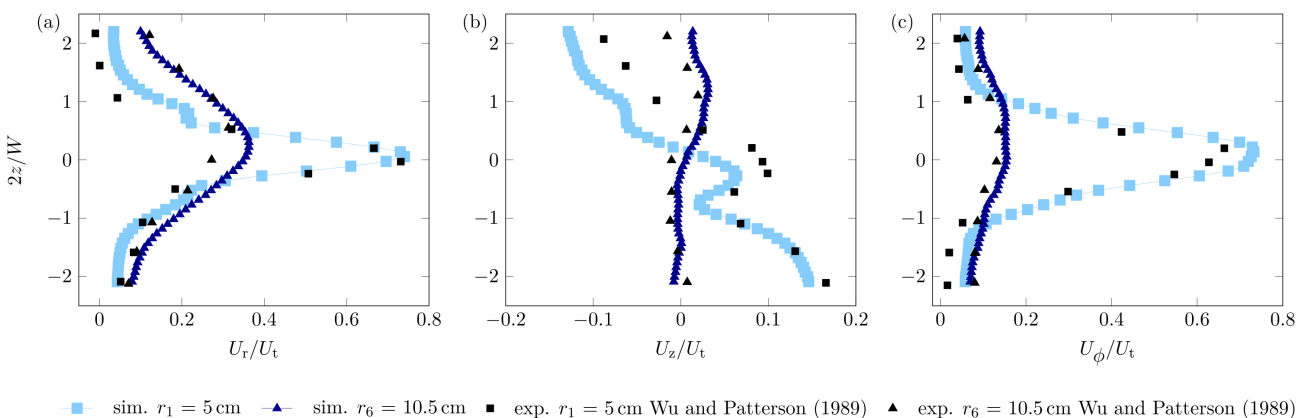

Figure 2. Comparison of the experimental results of Wu and Patterson [11] (black symbols) with the simulation results (blue symbols) of the velocity profiles for different radial positions: $r_1 = 5$ cm, $r_6 = 10.5$ cm. (a) Radial, (b) axial, and (c) tangential velocity components.

Chemical Engineering & Technology

3.2.2 Pitched-Blade Turbine

Fig. 3 shows the velocity profiles from experiments for two different axial positions as reported by Murthy and Joshi [30] and the CFD simulation results from this study. Slight deviations from the experimental results can be seen in Fig. 3a–c. The comprehensive comparison of simulation and experimental data for seven different positions is available in the Supporting Information. The highest dissipation rates occur in the impeller region, and higher dissipation extends below it toward the tank bottom.

3.4 Dissipation Rate and Trailing Vortex for Rushton Turbine

The dissipation rate is crucial for chemical processes, affecting mixing, reactions, and multiphase phenomena. It is discussed and compared with literature results in this section. First, the experimental data of Wu and Patterson [11] are discussed with Fig. 4. The x-axis represents the local dissipation rate normalized with the volume averaged dissipation rate $\varepsilon/\varepsilon_{avg,CFD}$ with $\varepsilon_{avg,CFD} = 0.1207\,\mathrm{m^2s^{-3}}$. Fig. 4a depicts the normalized local dissipation rate for the radial positions r_1 and r_6. For r_1, large deviations from the experimental results of Wu and Patterson are observable. The maximum in the simulation results is ca. 60 % higher than the largest experimental value. At $2z/W = 0$, where W is the blade width, the experimental value reaches $\varepsilon/\varepsilon_{avg} = 5$, as opposed to the simulation result of $\varepsilon/\varepsilon_{avg} = 22$. In contrast, for the r_6 position, the simulation predicts accurately the experimental results, as it does for r_2 and r_5 (Fig. 4b), as well as for r_3 and r_4 (Fig. 4c). Note that Wu and Patterson discuss in their work that the dissipation near the impeller is difficult to measure. Especially resolution issues but also data processing can have a dramatic effect on absolute, especially higher, dissipation rates found in experiments, which makes validation particularly challenging [36]. The observed dissipation rate at $r_1 = 5\,\mathrm{cm}$ presented in this study may be subject to measurement issues, as the data were collected at a distance of only 3.5 mm from the impeller blade. Additional investigations are done with further literature data.

Ng and Yianneskis described a method by which they calculated the distribution of the dissipation rate in the stirred tank and compared it to literature data [37]. The tank volume is divided into three regions:

1. Impeller swept volume: $0 < r < R$ and $\left(C - \frac{H}{2}\right) < z < \left(C + \frac{H}{2}\right)$, where r is the radial coordinate, R the radius, C the impeller clearance from the bottom, h the height, and z the axial coordinate.
2. Impeller stream volume: $R \leq r < 2R$ and $\left(C - \frac{H}{2}\right) < z < \left(C + \frac{H}{2}\right)$.
3. Remainder of the tank.

The percentages of the dissipation rate determined in each region of the tank are presented in Tab. 1 and compared to corresponding literature values.

Table 1. Comparison of estimates of ε distribution in vessels stirred by an RT reported in the literature (adapted from [37]) and updated with this study.

Ref.	Percentage of ε		
	Impeller swept region	Impeller stream region	Remainder of tank
[37]	12	31	57
[38]	20	50	20–40
[39]	–	38	–
[40]	60	–	–
[41]	30	30	40
[42]	30	34	36
[10]	54	35	11
[43]	36	30	34
[44]	30	30	40
[45]	15.3	28.2	–
[46]	18	60	22
This study	16	44	39

sim. $Z_1 = 0.01\,\mathrm{m}$ ▪ sim. $Z_3 = 0.082\,\mathrm{m}$ ▲ exp. $Z_1 = 0.01\,\mathrm{m}$ Murthy and Joshi (2008) ■ exp. $Z_3 = 0.082\,\mathrm{m}$ Murthy and Joshi (2008)
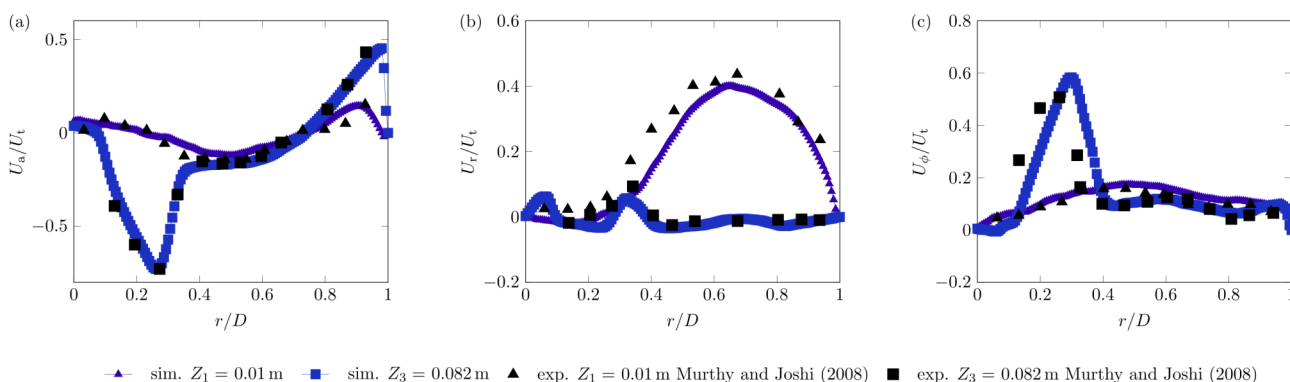
Figure 3. Comparison of the experimental results of Murthy and Joshi [30] (black symbols) with the simulation results (blue symbols) of the velocity profiles for different radial positions. (a) Axial, (b) radial, and (c) tangential velocity components for different axial positions in a stirred tank equipped with a PBT.
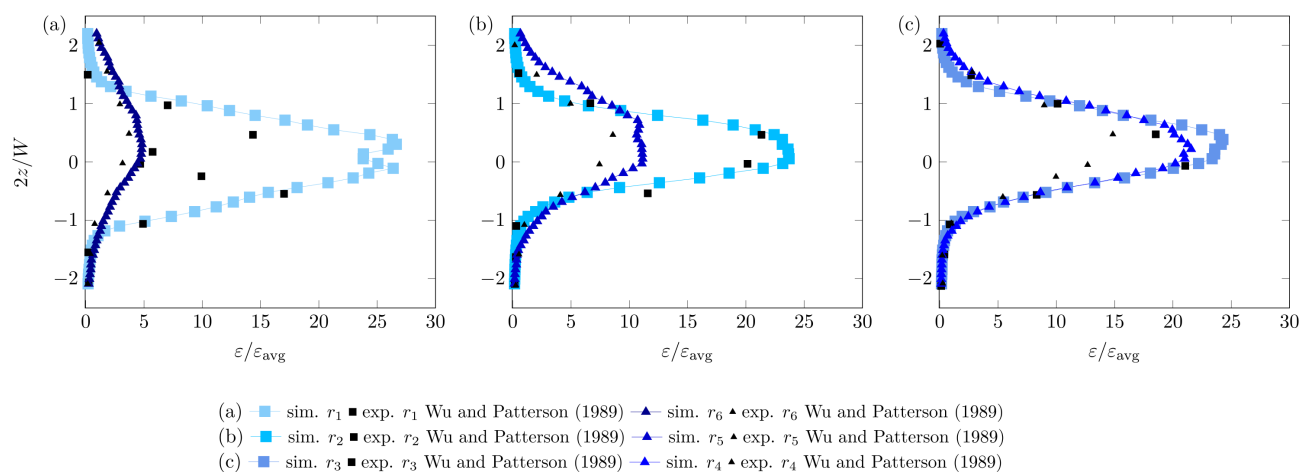
Research Article

Figure 4. Comparison of the experimental results of Wu and Patterson [11] (black symbols) with the simulation results (blue symbols) of the normalized dissipation rate $\varepsilon/\varepsilon_{avg}$ for different radial positions. (a) $r_1 = 5$ cm, $r_6 = 10.5$ cm; (b) $r_2 = 6$ cm, $r_5 = 9$ cm; (c) $r_3 = 7$ cm, $r_4 = 7.7$ cm.

Ng and Yianneskis noted that the regions presented in Tab. 1 are not similar in all studies, so that comparisons should be handled with caution. Furthermore, there are differences in geometries in the various studies, and these have an influence on the power number and dissipation rate. For example, Zhou and Kresta used a different tank-to-diameter ratio [45]. Nevertheless, Tab. 1 shows that there is a distribution of ε in different studies, especially in pioneering work. Ng and Yianneskis presented CFD data and located the largest dissipation (57 %) in the remainder of the tank [37]. In this study, the largest fraction of ε is in the impeller stream region, i.e., 44 %. The other studies, which used experimental data, located the largest share of the dissipation in the impeller swept regions. In contrast, Refs. [37, 45] and this study located the smallest share in this region. There are fundamental differences between this work and Ref. [37], which applied the Standard $k - \varepsilon$ RANS model instead of LES. Although Wu et al. presented an equivalent set-up, there are differences between the experimental results and the presented CFD results [44]. Experimental data are often extrapolated from data that are measured in one or a few locations of the tank, which can cause deviations. In addition, the CFD data deviate due to the turbulence modeling and the standard $k - \varepsilon$ RANS model being a more limited model. Compared with the study of Derksen and van den Akker, which also used LBM and LES for the CFD simulations, the deviations are much smaller [46]. This general trend is associated with the improving quality of both experimental and simulative techniques over the last 30 years.

Besides averaged dissipation values, some literature presents local maximum values. Zhou and Kresta showed that the maximum rate of dissipation ε_{max} is independent of the off-bottom clearance, impeller diameter, rotational speed, and number of baffles [45]. For an RT, they located ε_{max} at the tip of the impeller blades. At an impeller speed of 300 rpm, the maximum dissipation is 12.2, normalized with the diameter and the impeller speed. In this work, the normalized ε_{max} value is 34.91, and it is located at the tip of the impeller blades. This is still in the expected range of deviations originating from the dependence

on resolution and accuracy of turbulence modeling in CFD simulations. Obtaining three instantaneous velocity components over time $(\vec{u}(t), \vec{v}(t), \vec{w}(t))$ is challenging even with current methods. Accurate dissipation rate determination in stirred tanks is widely discussed in the literature, necessitating more precise measurement data for CFD model validation.

Finally, an additional characteristic of an RT are the trailing vortices, which are depicted in Fig. 5. Fig. 5a shows the mean axis of the trailing vortex according to different literature [47–50]. Whereas Ref. [49] used a photographic technique to find the shape of the vortex, Refs. [47, 48, 50] applied laser doppler anemometry mean velocity data to determine the central axis. The simulation results are depicted with green dots. Therefore, the upper and the lower vortex are considered individually. For evaluation, each vortex is superimposed to define the central axis. Fig. 5b depicts the simulated trailing vortex as an iso-surface colored with the velocity magnitude. These iso-surfaces were generated during the post-processing phase, by using volume data and employing the vorticity magnitude as the basis for their creation. The differences between these investigations are assigned to differences in the geometrical set-ups and the rotational speeds. Nevertheless, the simulated vortex is compared to the different experimental studies and is located in the range of other studies. Furthermore, the simulated vortex fits well into the experimental data and agrees with only slight deviations to the experimental results from [48].

3.3 Mixing Time

The mixing time predicted by CFD simulations is compared with experimental data from Jones and Ozcan-Taskin [7] for a stirred tank reactor equipped with an impeller with four pitched blades. In the experiments, three conductivity probes were used to determine the mixing time, which was replicated in the simulations; see Sect. S2 for a visualization and further details. In this work, two tanks were investigated, i.e., PBT-T31 and PBT-T61 in Tab. S1. As bulk liquid, water ($\rho_b = 1000$ kg m^{-3},
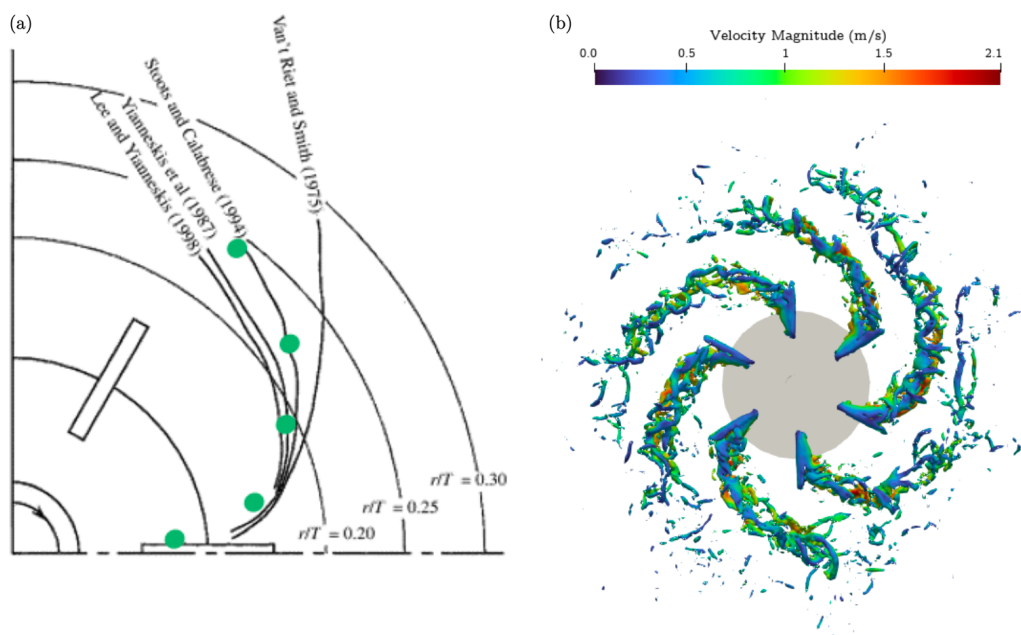
Figure 5. Representation of the trailing vortex in an RT-equipped stirred tank reactor. (a) Centered axis of the trailing vortex according to different authors (modified from [47]) combined with this study and (b) simulated trailing vortex presented as iso-surfaces for $Re = 28\,830$. T is the tank diameter.

$\mu_b = 0.001$ Pa s) was used. A glucose solution of different viscosity was added with a liquid content of 0.15 % in relation to the total tank volume at a position close to the liquid surface (see Sect. 2).

Fig. 6 shows the mixing time Θ evaluated by the RMS criterion versus stirrer speed N for the simulations (blue symbols) and the experiments (black symbols) from Ref. [7] for different viscosities of the tracer, i.e., 0.001, 0.5, 2.9, and 10 Pa s, and for two different tank geometries (empty and filled symbols). Greenville suggests approximating the 95 % mixing time in a stirred tank reactor with the following equation [51], which is also added to this figure as a dashed line [Eq. (13)]:

$$\Theta = 5.2\left(\frac{1}{N}\right)\left(\frac{1}{Po}\right)^{1/3}\left(\frac{T}{D}\right)^2 \tag{13}$$

where T is the tank diameter.

For small viscosity differences between the tank liquid and the dosed liquid, only small deviations between experiments and CFD simulations occur. Contrarily, large deviations are present between the experiments and the simulations for large viscosity differences, especially at medium stirrer speeds. One reason might be that in the experiments, a syringe is used to add the high-viscosity fluid slightly above the liquid surface, whereas in the CFD simulations, the tracer is added already below the liquid surface. The simulation results did not capture the small diameter of the syringe, as it would probably require a very fine grid resolution that was not feasible due to hardware limitations. It is theoretically possible to perform local grid refinement in arbitrary regions, e.g., in the injection region. This local refinement has the advantage that the grid spacing can be reduced without significantly increasing the time for grid generation, while maintaining a regular grid structure. Since this cannot be fully clarified, more research is needed to elucidate the mixing between liquids with different viscosities. In the Supporting Information, the transient concentration
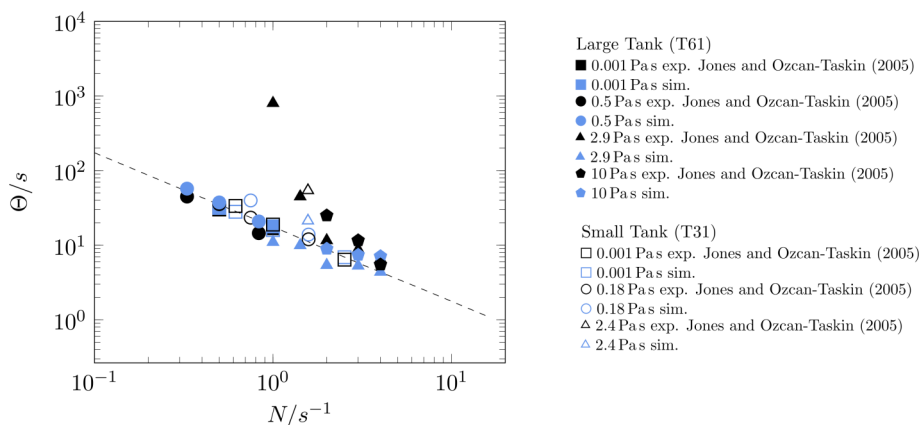

Large Tank (T61)
■ 0.001 Pa s exp. Jones and Ozcan-Taskin (2005)
■ 0.001 Pa s sim.
● 0.5 Pa s exp. Jones and Ozcan-Taskin (2005)
● 0.5 Pa s sim.
▲ 2.9 Pa s exp. Jones and Ozcan-Taskin (2005)
▲ 2.9 Pa s sim.
⬟ 10 Pa s exp. Jones and Ozcan-Taskin (2005)
⬟ 10 Pa s sim.

Small Tank (T31)
□ 0.001 Pa s exp. Jones and Ozcan-Taskin (2005)
□ 0.001 Pa s sim.
○ 0.18 Pa s exp. Jones and Ozcan-Taskin (2005)
○ 0.18 Pa s sim.
△ 2.4 Pa s exp. Jones and Ozcan-Taskin (2005)
△ 2.4 Pa s sim.

Figure 6. Mixing time evaluated by RMS criterion for added liquids with high and low viscosity differences in two tank dimensions (empty symbols for small tank, filled symbols for large tank). Experimental values in black from [7], CFD results in blue. The dashed line represents the correlation of Eq. (12).

fields are visualized. Nevertheless, the good agreement of experimental and computational mixing times up to viscosity ratios of 1:100 is of use for industrial applications, as such cases are highly relevant for stirred tank design. The ease of use of the software therefore allows for quick and reliable design calculations in this regime.

4 Conclusion

Mixing in stirred tank reactors is a common but complex operation in the chemical and process industry. Reliable models are needed, e.g., for scale-up purposes. With improved physics in CFD simulations, such as LES turbulence models, turbulent mixing can be efficiently modeled, especially if they are run on GPUs. In this study, LES CFD simulations were carried out to evaluate the current state and to highlight the need for further research in this field. LBM has certain advantages over FVM. The rapid generation of a regular grid is significantly more efficient than the demanding task of creating an optimal mesh in FVM. Additionally, the swift grid generation enables effective discretization, facilitating the use of LES models instead of RANS. Furthermore, when harnessed with the robust capabilities of GPUs, simulations run at an accelerated pace.

First, the power characteristics of a crossbar, RT, helical ribbon, and anchor impeller were tested in different flow regimes and compared with experimental data from Zlokarnik [29]. It was shown that the CFD simulation results differ only slightly from the reported experiments. Second, an RT and a PBT were validated in detail, which included a lattice study for flow fields, the velocity components, and dissipation rates. Moreover, the trailing vortex of the RT was also simulated and compared with literature results. Regarding the lattice resolution, a good starting point is to use 100 points over the impeller diameter. Finally, mixing times for different viscosity ratios were determined from the CFD results and compared with a literature study [7]. It was shown that mixing times for viscosity ratios up to 1:100 could be predicted with small deviations. In contrast, it was observed that when a high-viscosity fluid was added, the simulated mixing time did not match the experimental one, although mass was fully conserved. The reason might be found either in a different adding procedure in the simulation or more fundamental physics cannot be modeled by using the current approaches. This is also a known issue in classic CFD, and more basic research combining detailed experiments with high-resolution CFD simulations is needed.

Supporting Information

Acknowledgment

Symbols used

a	[m s^{-1}]	particle velocity
c	[–]	normalized probe output
c_s	[m s^{-1}]	constant velocity
Co	[–]	Courant number
C	[m]	impeller clearance from bottom
D	[m]	impeller diameter
f	[–]	distribution function of the particles
f_i^*	[–]	distribution after collision
f_1^{eq}	[–]	equilibrium distribution
F	[kg m s^{-2}]	force
H	[m]	height
M	[Nm]	torque
N	[min^{-1}]	impeller speed
p	[kg s^{-2}m^{-1}]	pressure
P	[W]	power input
Po	[–]	power number
r	[m]	radial coordinate
R	[m]	radius
Re	[–]	Reynolds number
T	[m]	tank diameter
t	[s]	time
u	[m s^{-1}]	velocity
U	[m s^{-1}]	velocity
W	[m]	blade width
x	[–]	position/location
z	[m]	axial coordinate

Greek letters

α	[–]	volume fraction
ε	[m^{2}s^{-3}]	dissipation rate
θ	[m]	mixing time
ν	[m^{2}s^{-1}]	kinematic viscosity
μ	[Pa s]	dynamic viscosity
ν	[m^{2}s^{-1}]	kinematic viscosity
ξ	[m s^{-1}]	Velocity
ρ	[kg m^{-3}]	density
σ	[–]	variance
τ	[s]	relaxation time
Ω	[kg s m^{-3}]	collision operator

Sub- and superscripts

avg	average
b	bulk
β	direction
CFD	computational fluid dynamics
ϕ	tangential
max	maximum
r	Radial
RMS	root mean square
t	tip
z	axial

Abbreviations

CFD	computational fluid dynamics
FVM	finite volume method

GPU   graphics processing unit
LBM   lattice Boltzmann method
LES   large eddy simulation
PBT   pitched-blade turbine
RANS   Reynolds-averaged Navier-Stokes
RMS   root mean square
RT   Rushton turbine
VoF   volume of fluid

References

[1] A. W. Nienow, *Chem. Ing. Tech.* **2014**, *86 (12)*, 2063–2074. DOI: https://doi.org/10.1002/cite.201400087

[2] D. F. Fletcher, *Chem. Eng. Res. Des.* **2022**, *187*, 299–305. DOI: https://doi.org/10.1016/j.cherd.2022.09.021

[3] G. Ascanio, *Chin. J. Chem. Eng.* **2015**, *23 (7)*, 1065–1076. DOI: https://doi.org/10.1016/j.cjche.2014.10.022

[4] M. Barigou, *Chem. Eng. Res. Des.* **2004**, *82 (9)*, 1258–1267. DOI: https://doi.org/10.1205/cerd.82.9.1258.44160

[5] A. W. Patwardhan, J. B. Joshi, *Ind. Eng. Chem. Res.* **1999**, *38 (8)*, 3131–3143. DOI: https://doi.org/10.1021/ie980772s

[6] R. K. Grenville, A. T. C. Mak, D. A. R. Brown, *Chem. Eng. Res. Des.* **2015**, *100*, 282–291. DOI: https://doi.org/10.1016/j.cherd.2015.05.026

[7] P. N. Jones, G. N. Ozcan-Taskin, *Chem. Eng. Technol.* **2005**, *28 (8)*, 908–914. DOI: https://doi.org/10.1002/ceat.200500012

[8] M. Liu, *Chem. Eng. Sci.* **2012**, *69 (1)*, 382–393. DOI: https://doi.org/10.1016/j.ces.2011.10.062

[9] S. Kresta, *Can. J. Chem. Eng.* **1998**, *76 (3)*, 563–576. DOI: https://doi.org/10.1002/cjce.5450760329

[10] S. M. Kresta, P. E. Wood, *AIChE J.* **1991**, *37 (3)*, 448–460. DOI: https://doi.org/10.1002/aic.690370314

[11] H. Wu, G. K. Patterson, *Chem. Eng. Sci.* **1989**, *44 (10)*, 2207–2221. DOI: https://doi.org/10.1016/0009-2509(89)85155-3

[12] J. H. Ferziger, M. Perić, R. L. Street, *Computational Methods for Fluid Dynamics*, 4th ed., Springer, Berlin, Heidelberg **2020**.

[13] M. Wu, N. Jurtz, A. Walle, M. Kraume, *Chem. Eng. Sci.* **2022**, *263*, 118109. DOI: https://doi.org/10.1016/j.ces.2022.118109

[14] R. O. Fox, in *Advanced Approaches in Turbulence* (Ed: P. Durbin), Elsevier **2021**, 307–371.

[15] S. Chen, G. D. Doolen, *Annu. Rev. Fluid Mech.* **1998**, *30 (1)*, 329–364. DOI: https://doi.org/10.1146/annurev.fluid.30.1.329

[16] J. Derksen, *Chem. Eng. Res. Des.* **2001**, *79 (8)*, 824–830. DOI: https://doi.org/10.1205/02638760152721334

[17] C. K. Aidun, J. R. Clausen, *Annu. Rev. Fluid Mech.* **2010**, *42 (1)*, 439–472. DOI: https://doi.org/10.1146/annurev-fluid-121108-145519

[18] T. Krüger, H. Kusumaatmaja, A. Kuzmin, O. Shardt, G. Silva, E. M. Viggen, *The Lattice Boltzmann Method: Principles and Practice*, 1st ed. 2017 ed., Springer International Publishing: Imprint: Springer, Cham **2017**.

[19] Kevinstratford, O. Henrich, Jlintuvuori, Dmarendu, Qikaifzj, ShanCHEN123, Ludwig-Cf, Jurijsab, Slevinskygra, Ludwig 0.20.1, Zenodo, **2023**. DOI: https://doi.org/10.5281/ZENODO.8125118

[20] C. Godenschwager, F. Schornbaum, M. Bauer, H. Köstler, U. Rüde, in *Proc. Int. Conf. High Perform. Comput. Netw. Storage Anal.*, ACM, Denver Colorado **2013**.

[21] J. Latt, O. Malaspinas, D. Kontaxakis, A. Parmigiani, D. Lagrava, F. Brogi, M. B. Belgacem, Y. Thorimbert, S. Leclaire, S. Li, F. Marson, J. Lemus, C. Kotsalos, R. Conradin, C. Coreixas, R. Petkantchin, F. Raynaud, J. Beny, B. Chopard, *Comput. Math. Appl.* **2021**, *81*, 334–350. DOI: https://doi.org/10.1016/j.camwa.2020.03.022

[22] A. Kummerländer, S. Avis, H. Kusumaatmaja, F. Bukreev, M. Crocoll, D. Dapelo, N. Hafen, S. Ito, J. Jeßberger, J. E. Marquardt, J. Mödl, T. Pertzel, F. Prinz, F. Raichle, M. Schecher, S. Simonis, D. Teutscher, M. J. Krause, OpenLB Release 1.6, Zenodo, **2023**. DOI: https://doi.org/10.5281/ZENODO.7773497

[23] H. Xu, P. Sagaut, *J. Comput. Phys.* **2011**, *230 (13)*, 5353–5382. DOI: https://doi.org/10.1016/j.jcp.2011.03.040

[24] R. Schäfer, M. Böhle, *Acoustics* **2020**, *2 (4)*, 735–752. DOI: https://doi.org/10.3390/acoustics2040040

[25] Y. Feng, J. Miranda-Fuentes, S. Guo, J. Jacob, P. Sagaut, *J. Adv. Model. Earth Syst.* **2021**, *13 (3)*. DOI: https://doi.org/10.1029/2020MS002107

[26] Z. Lu, Y. Liao, D. Qian, J. B. McLaughlin, J. J. Derksen, K. Kontomaris, *J. Comput. Phys.* **2002**, *181 (2)*, 675–704. DOI: https://doi.org/10.1006/jcph.2002.7151

[27] H. Hartmann, J. J. Derksen, H. E. A. Van Den Akker, *AIChE J.* **2004**, *50 (10)*, 2383–2393. DOI: https://doi.org/10.1002/aic.10211

[28] J. J. Giacomelli, H. E. A. Van den Akker, *Flow Turbul. Combust.* **2020**, *105 (1)*, 31–62. DOI: https://doi.org/10.1007/s10494-019-00095-z

[29] M. Zlokarnik, *Rührtechnik*, Springer Berlin Heidelberg, Berlin, Heidelberg **1999**.

[30] B. N. Murthy, J. B. Joshi, *Chem. Eng. Sci.* **2008**, *63 (22)*, 5468–5495. DOI: https://doi.org/10.1016/j.ces.2008.06.019

[31] J. Smagorinsky, *Mon. Weather Rev.* **1963**, *91 (3)*, 99–164. DOI: https://doi.org/10.1175/1520-0493(1963)091<0099:GCEWTP>2.3.CO;2

[32] H. Yu, S. S. Girimaji, L.-S. Luo, *J. Comput. Phys.* **2005**, *209 (2)*, 599–616. DOI: https://doi.org/10.1016/j.jcp.2005.03.022

[33] C. W. Hirt, B. D. Nichols, *J. Comput. Phys.* **1981**, *39 (1)*, 201–225. DOI: https://doi.org/10.1016/0021-9991(81)90145-5

[34] E. L. Paul, V. A. Atiemo-Obeng, S. M. Kresta, *Handbook of Industrial Mixing*, John Wiley & Sons, Inc, Hoboken, NJ **2003**.

[35] V. Roussinova, S. M. Kresta, *Ind. Eng. Chem. Res.* **2008**, *47 (10)*, 3532–3539. DOI: https://doi.org/10.1021/ie070955r

[36] A. Gabriele, A. W. Nienow, M. J. H. Simmons, *Chem. Eng. Sci.* **2009**, *64 (1)*, 126–143. DOI: https://doi.org/10.1016/j.ces.2008.09.018

[37] K. Ng, M. Yianneskis, *Chem. Eng. Res. Des.* **2000**, *78 (3)*, 334–341. DOI: https://doi.org/10.1205/026387600527446

[38] L. A. Cutter, *AIChE J.* **1966**, *12 (1)*, 35–45. DOI: https://doi.org/10.1002/aic.690120110

[39] A. A. Günkel, M. E. Weber, *AIChE J.* **1975**, *21 (5)*, 931–939. DOI: https://doi.org/10.1002/aic.690210515

[40] I. Fořt, J. Drbohlav, J. Krátký, M. Grospičová, Z. Kroužilová, *Collect. Czechoslov. Chem. Commun.* **1972**, *37 (1)*, 222–240. DOI: https://doi.org/10.1135/cccc19720222

[41] H. D. Laufhutte, A. Mersmann, in *Proc. Fifth European Conf. on Mixing*, Würzburg, Germany **1985**.

[42] V. V. Ranade, J. B. Joshi, *Chem. Eng. Commun.* **1989**, *81 (1)*, 197–224. DOI: https://doi.org/10.1080/00986448908940539

[43] A. Togatorop, *Ph.D. Thesis*, UMIST **1995**.

[44] H. Wu, G. K. Patterson, M. Van Doorn, *Exp. Fluids* **1989**, *8 (3–4)*, 153–160. DOI: https://doi.org/10.1007/BF00195789

[45] G. Zhou, S. M. Kresta, *AIChE J.* **1996**, *42 (9)*, 2476–2490. DOI: https://doi.org/10.1002/aic.690420908

[46] J. Derksen, H. E. A. van den Akker, *AIChE J.* **1999**, *45 (2)*, 209–221. DOI: https://doi.org/10.1002/aic.690450202

[47] K. C. Lee, M. Yianneskis, *AIChE J.* **1998**, *44 (1)*, 13–24. DOI: https://doi.org/10.1002/aic.690440104

[48] C. M. Stoots, R. V. Calabrese, *AIChE J.* **1995**, *41 (1)*, 1–11. DOI: https://doi.org/10.1002/aic.690410102

[49] K. Van't Riet, J. M. Smith, *Chem. Eng. Sci.* **1975**, *30 (9)*, 1093–1105. DOI: https://doi.org/10.1016/0009-2509(75)87012-6

[50] M. Yianneskis, Z. Popiolek, J. H. Whitelaw, *J. Fluid Mech.* **1987**, *175 (1)*, 537. DOI: https://doi.org/10.1017/S002211208700051X

[51] R. K. Greenville, *Ph.D. Thesis*, Cranfield University **1992**.

Research Article: There is a need for reliable models of mixing in stirred tanks, which is widely used in the chemical and process industry but complex and not fully understood. A lattice Boltzmann code with a large eddy simulation turbulence model was used to determine power numbers and mixing times in stirred tanks with different impellers. Local velocity fields and dissipation rates were compared with literature data.

Simulating Stirred Tank Reactor Characteristics with a Lattice Boltzmann CFD Code

Jule Kersebaum, Steffen Flaischlen, Julia Hofinger, Gregor D. Wehinger*

Supporting Information available online